

In situ observation of interactive failure modes in a single-edge notched symmetric cross-ply laminate using synchrotron X-ray tomography

Eonyeon Jo^{1,2}, Sooyoung Lee¹, Chaeyoung Hong, Wooseok Ji*

Department of Mechanical Engineering, Ulsan National Institute of Science and Technology (UNIST), Ulsan, South Korea

ARTICLE INFO

Keywords:
 Synchrotron radiation computed tomography
In situ testing
 Interactive fracture behavior
 DIC analysis

ABSTRACT

Interactive failure mechanisms of a single-edge notched (SEN) symmetric cross-ply laminate subjected to tensile loading are studied *in situ* using synchrotron X-ray tomography and a DIC technique at the micro- and macro-scales. The SEN configuration guarantees the repeatability and consistency of the progressive and interactive failure behavior at the two different scales. The evolution of various fracture modes in different layers is observed through synchrotron radiation CT images. Due to the geometrically asymmetric configuration, all the initial cracks sequentially occurring near the notch tip can be captured in a narrow field of view. Stress relaxation due to the subsequent fracture initiations is indirectly captured by measuring the crack lengths and opening displacements from the 3D CT images at different loading steps. The stress relaxation is directly measured by DIC analysis using the macro-scale test data. DIC results show strains relaxed in the region between existing and emerging transverse cracks.

1. Introduction

Composite materials have been typically used in aerospace applications due to the lightweight advantages that the material system can offer. Recently, automotive industry is greatly interested in using the composites to reduce vehicle weight in response to the strengthening regulation on fuel consumptions and air pollutant emissions [1]. While the composite material is one of the best candidates for lightweight vehicles, it is crucial to have a good understanding of its unique failure behavior to design a safe load-bearing structure. Fiber-reinforced composite structures are well known to suffer from various types of damage at multiple length scales. Typical failure modes found at the fiber level are matrix microcracking, fiber/matrix debonding, and fiber kinks, mainly resulting from the huge stiffness mismatch between fibers and a matrix material. These micro-failure modes may be initiated even at a very low stress in terms of a globally applied load since local stress concentration may occur in the heterogeneous microstructure. The micro-scale damage is mainly responsible for the degradation of the mechanical properties of the composite material [2]. Furthermore, with increasing load, they may transform into a larger scale mode of failure such as transverse matrix cracks at the meso-length scale and delamination at the macro-length scale. Indeed, the micro-scale damage initiation can potentially be a significant threat to the entire structural

system. In order to have a better understanding of how a composite structure fails, it is required to closely examine the initiation and growth of various failure modes at the micro-length scale.

Detailed failure progression from the initiation of micro-damage to the catastrophic failure at the macroscopic scale is extremely difficult to obtain without a special testing instrument equipped with a microscopic device. Digital image correlation (DIC) technique is now widely used to investigate the progressive damage and failure response of a composite material in real time. However, the information from DIC analysis is limited to surfaces where speckle patterns are applied [3]. Although many researches have been performed to study progressive damage and failure behavior in composite materials, *ex situ* approaches are typically employed to observe microscopic failure patterns at different loading stages [4,5]. Progression of damage and failure is often characterized by indirect measurements such as acoustic emission (AE) data [6–8]. However, conventional *ex situ* and non-destructive testing protocols are insufficient to obtain detailed information about the initiation of various failure modes and their interactive mechanisms since the micro-failure modes are initiated and growing inside of the materials.

With the increasing interest in the observation of subsurface failure behavior in composite materials and owing to the development of computational tomography resources, 3D X-ray micro-computed

* Corresponding author.

E-mail address: wsji@unist.ac.kr (W. Ji).

¹ Both authors contributed equally to this manuscript.

² Currently at LG Hausys R&D Center, Seoul, South Korea.

Table 1

Mechanical properties of the UIN150/H15 composite material.

	Properties	Values	Layup	ASTM Standard
Stiffness [GPa]	Fiber direction (E_1)	146.45 ± 2.25	[0 ₈] _T	D3039
	Transverse direction (E_2)	7.439 ± 0.047	[90 ₈] _T	D3039
	Poisson's ratio (ν_{12})	0.338 ± 0.050	[0 ₈] _T	D3039
	Shear (G_{12})	4.15 ± 0.40	[+45 ₂ /−45 ₂] _S	D3518
Strength [MPa]	Fiber direction (X)	2672.24 ± 83.61	[0 ₈] _T	D3039
	Transverse direction (Y)	26.26 ± 2.24	[90 ₈] _T	D3039
	Shear (S)	43.811 ± 1.151	[+45 ₂ /−45 ₂] _S	D3518
Fracture Toughness [N/mm]	Mode I (G_{IC})	0.1696 ± 0.02	[0 ₈] _T	D6671
	Mode II (G_{IIC})	3.269 ± 0.220	[0 ₈] _T	D7905

tomography (μ CT) has been utilized recently to visualize microstructural behavior in composite materials. X-ray tomography has evolved into a powerful imaging tool in the fields of physical and biological sciences due to its ability to image a structure in three dimensions with high spatial resolution at macroscopic to submicroscopic scales [9,10]. Buffiere et al. compared advantages and limitations of laboratory-scale and synchrotron X-ray sources for *in situ* thermal/mechanical testing [11]. The team of Spearing performed tensile tests on [90/0]_S laminates using a synchrotron X-ray source and revealed the progression of different failure modes and their interactions [12–14]. Garcea et al. further developed the work by applying fatigue loading on the specimens with the same configuration [15]. Hufenbach et al. built a laboratory-scale X-ray tomography system and carried out tension and compression tests on woven composite [16]. Bale et al. observed failure events in ceramic matrix composites under combined mechanical and elevated temperature loading using a synchrotron X-ray [17]. Sket et al. utilized ± 45° carbon fiber reinforced laminates to investigate damage progression in matrix [18]. Recently, a number of studies using X-ray CT to *in situ* observe damage behavior occurring inside composite materials have been reviewed in [19] and [20].

As pointed out in [19], X-ray CT images are instrumental to develop numerical models with a better understanding of damage mechanisms of the composites. However, most experimental results reported in the literature may be insufficient to validate their predictive capabilities after the first failure is initiated. In order for a numerical model to reproduce the full failure progression observed from the *in situ* technique, the numerical model should be modeled as a duplicate of the corresponding real microstructure, which significantly increases a complexity of the model. Such a numerical model would be practical to have a better understanding of the damage mechanisms of the test data, but its predictive capability for other situations would not be guaranteed due to different microstructural characteristics. Most experiments reported in [19] and [20] are valid for the failure initiation but the forthcoming damage behavior is heavily dependent on the microstructural characteristics of individual specimens, which is quite unique and random from specimens to specimens. For example, in the case of double-edge notched (DEN) specimens, when a crack is initiated from one of the notches, subsequent cracks may occur either the same side or the opposite side of the first crack. The progressive failure behavior in the DEN specimen is greatly influenced by the stochastic nature of the microstructure and may not be repeatedly obtained from multiple tests. Since initial cracks at the micro-length scale may not significantly affect the global response of composite structures until they grow sufficiently and interact with other failure modes, it is critical to have progressive damage behavior that can be repeatedly observed. Experimental data insensitive to specimen-specific parameters such as voids, manufacturing-induced defects, fiber misalignment and so on, therefore, should be required.

In this paper, we select the single-edge notched (SEN) symmetric cross ply laminate for a test specimen to study its failure behavior with emphasis on the interactive mechanisms of various damage modes,

typically found in composite materials. Tension tests on the SEN specimens are performed at the micro- and macro-scales. The specific specimen configuration, especially with the single-edge notch, produces repeatable failure progression even at the two different scales. The stacking sequence is particularly chosen to see common yet multiple failure modes from different layers and their interactions. The single-edge notch is introduced to the specimen in order to know the location of failure initiation *a priori* and reduce the stochastic dependence of subsequent cracking behavior. Synchrotron X-ray microtomography is utilized to specifically observe the evolution of various cracks near the notch tip. In addition to the observation, the crack lengths and crack opening displacements from the 3D CT images at different loading steps are measured to understand the interactive behavior of the cracks. The variance of strains due to the progression of multiple cracks is directly computed from the macro-scale SEN test data through DIC analysis. In the following sections, details about the specimens, experimental setup and test results will be presented.

2. Test specimens

2.1. Material properties of the specimens

The present study considers unidirectionally continuous carbon fibers embedded in an epoxy material. Prepregs with the material system of UIN150/H15 (SK Chemicals, South Korea) were utilized to fabricate test specimens. The prepregs had the fiber areal weight of 150 g/m², resulting in 40% of the fiber volume fraction approximately. Laminated composite panels with the stacking sequences of [0₈]_T, [90₂/0₂]_S, [+45₂/−45₂]_S and [0₃₂]_T were first manufactured to measure the basic mechanical properties of the composite system based on ASTM testing standards. The measured material properties with the corresponding layups and standard documents used for the measurements are listed in Table 1.

2.2. Single edge notched specimen

In the present study, single-edge notched (SEN) specimens having the stacking sequence of [90₂/0₂]_S are utilized to scrutinize the interactive failure behavior of the symmetric cross-ply laminates. Fig. 1 shows the configuration of the SEN specimens and the dimensions for two different testing setups are summarized in Table 2. Fig. 2(a) compares the specimen sizes for the two different tests. The specimens are cut from the same panels of symmetric cross-ply laminates with the thickness of 1.1 mm. The notches are carved using a fine-resolution CNC waterjet with the nozzle size of 0.35 mm. A typical notch tip surface is shown in Fig. 2(b), which shows no particular flaw. Fig. 3 schematically illustrates the tension test setup. Fiber orientations of each layer are exhibited with respect to the loading direction. In the present study, 90-degree layers are intentionally placed outside to perform DIC analysis on the surface that is to fail first.

Although the cross-ply laminates have been experimentally studied

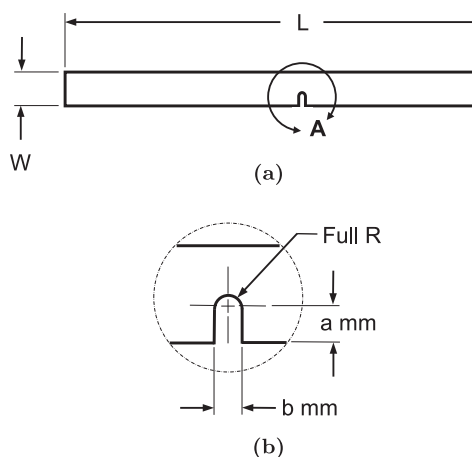


Fig. 1. (a) Dimensions of the single edge notched specimen, (b) detailed view of the notch.

Table 2
Specimen dimensions for *in situ* and macroscale tests.

L (mm)	W (mm)	a (mm)	b (mm)	Remark
70	5	1.7	0.6	<i>In situ</i> test
160	20	3.7	0.6	Macroscale test

using synchrotron radiation by many researchers [12–15], all of the specimens had notches on both sides. For *in situ* experiments, notches are generally necessary in order to locally increase stresses and regulate the initiation of failure in the region. However, once a crack is initiated at one of the notches in a double-edge notched (DEN) specimen, the symmetry of the specimen is immediately destroyed. As a result, types and locations of the next failures are completely subjective to the current stress state of the fractured double-notched area, which cannot be repeatedly obtained due to the stochastic nature of the heterogeneous microstructure. Specimens with geometrically asymmetric configuration may be more appropriate to have a refined cluster of multiple

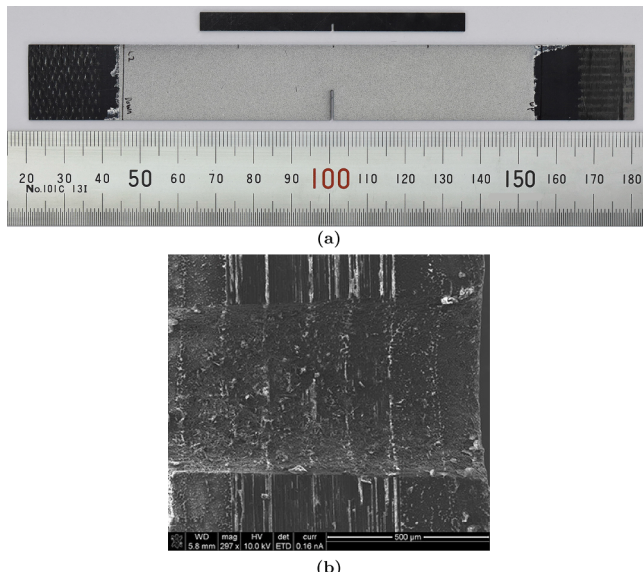


Fig. 2. (a) Microscopic and macroscopic test specimens. For the macroscopic specimen, the speckle pattern is applied on the surface to perform DIC analysis. (b) Microscopic observation of the notch tip surface. (For interpretation of the references to colour in this figure legend, the reader is referred to the web version of this article.)

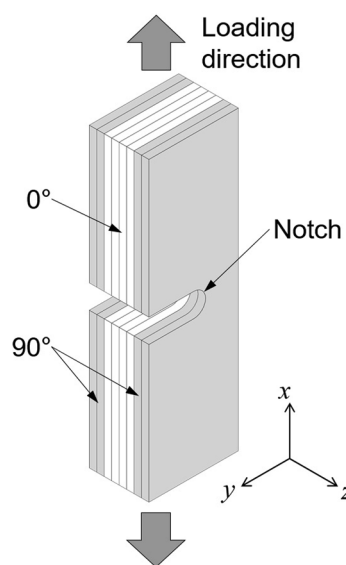


Fig. 3. Schematic illustration of the SEN test setup with the fiber orientations in each layer of the [90₂/0₂]_S specimen.

failure modes in a limited area and thus have a better understanding of interactive failure mechanisms [21]. Furthermore, since numerical models typically have a symmetric configuration [22], the non-symmetric failure behavior obtained from the double-notch tension tests may be inappropriate to validate their predictive capabilities.

3. SEN tests at the macro-length scale

Macro-scale tension tests on SEN specimens were first performed with a digital image correlation (DIC) technique to check the reproducibility of test results, especially the fracture behavior in the notch area. Instron 5982, electromechanically driven loading frame, was used to perform the tensile tests at the loading rate of 0.5 mm/min. The SEN specimens were held with wedge grips and images were taken during the test for DIC analysis. Fig. 4 shows the stress-strain curves of the macro-scale SEN specimens. The axial stresses are computed from the load cell data divided by the cross-sectional area at the notch. The

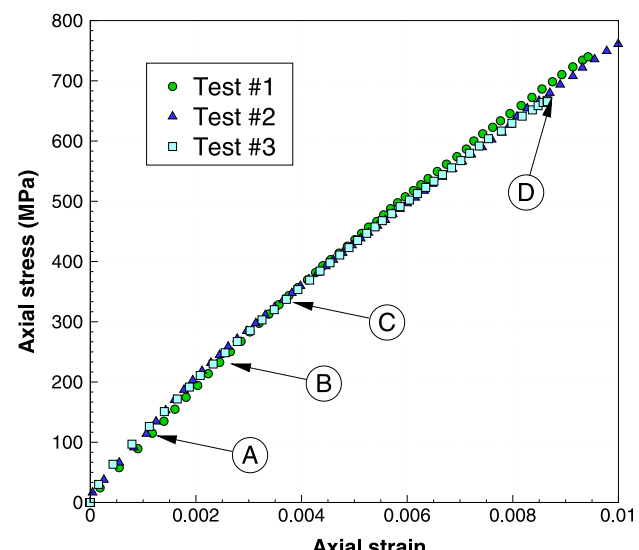


Fig. 4. Stress-strain curves of SEN specimens tested at the macro-length scale. DIC analysis results associated with loading stages A through D are shown in Fig. 5. (For interpretation of the references to colour in this figure legend, the reader is referred to the web version of this article.)

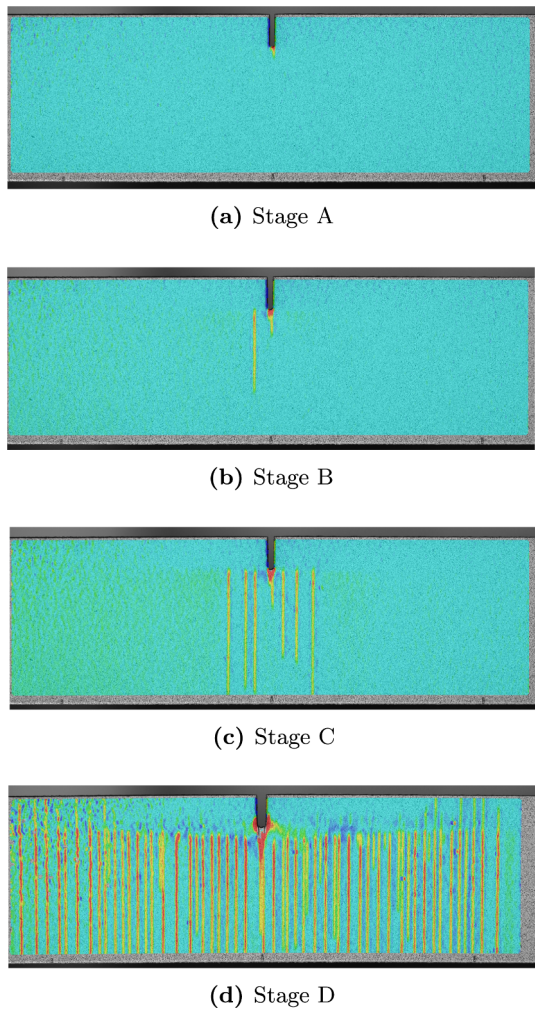


Fig. 5. Progression of transverse cracks on the 90° layer visualized by the DIC technique. Each stage is corresponding to specific location of the stress-strain curves as indicated in Fig. 4. (For interpretation of the references to colour in this figure legend, the reader is referred to the web version of this article.)

axial displacement data from the DIC analysis divided by the gage length is defined as the axial strains in Fig. 4. As can be seen in Fig. 4, the stress-strain data from different specimens are fairly consistent. Fig. 5 shows typical DIC results of loading-direction strains at different loading stages as indicated in Fig. 4. Fig. 6 shows the detailed progression of multiple cracks near the notch region. As can be seen in Fig. 6(a), a crack is initiated at the notch tip and the potential location of the next crack is indicated with the red dotted circle. The second crack emerges from the location and rapidly grows as shown in Fig. 6(b), while the first crack is not growing further. This implies the interaction between the two cracks, indirectly captured through the DIC analysis. It is also interesting to note that the DIC analysis is able to compute relaxed strains (blue color) around the cracks. The relaxation is more clearly observed in Fig. 6(c) between the first and third cracks. It is observed that, once stresses are relaxed, existing cracks are not growing anymore, but the regions outside the relaxation are strained more (red dotted circles in Fig. 6(a) and (c)). As a result, additional cracks are initiated and the stress relaxation in the region between the new and existing cracks are again observed from the DIC results. This interactive failure pattern is consistently observed from multiple tests. However, DIC results are limited on the surface where the speckle pattern is applied. The transverse cracks on the 90° layers may interact with other failure modes in 0° layer, which cannot be detected from the DIC technique.

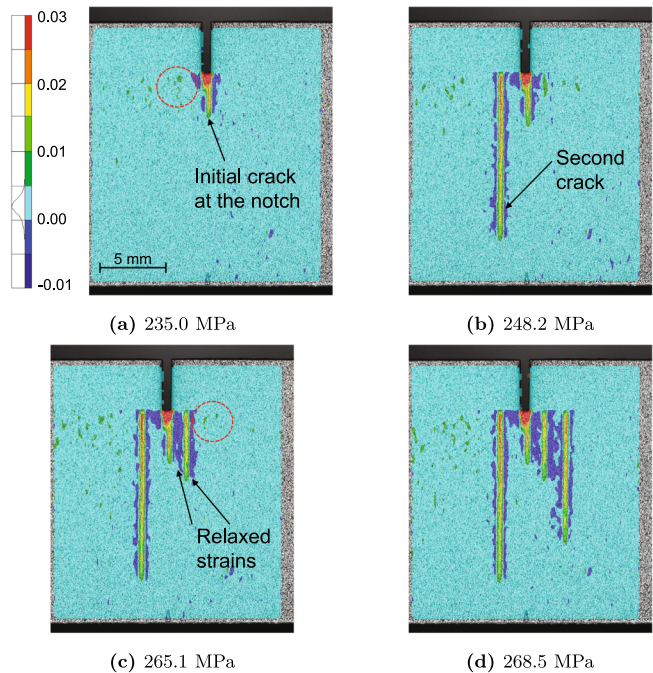


Fig. 6. Strain relaxation with the emergence of new cracks. (For interpretation of the references to colour in this figure legend, the reader is referred to the web version of this article.)

4. Experimentation at a synchrotron facility

4.1. In situ tensile testing device

In situ mechanical testing coupled with synchrotron X-ray tomography generally requires a special load frame that should be built within certain limitations particularly determined by the laboratory configurations at each synchrotron facility. The present loading device was specifically designed to be mounted on a high precision rotation stage installed in the X-ray tomography beamline (Beamline 6C) at Pohang Accelerator Laboratory (PAL). The height of the loading device was determined according to the position of the X-ray beam path in Beamline 6C. Incorporating other design requirements and limitations, the small-scale load frame as shown in Fig. 7 was fabricated. The device weighed around 9 kg and situated the center of the specimen at around 730 mm above the bottom.

As can be seen in Fig. 7, the polymethyl methacrylate (PMMA) tube was enclosing the specimen to protect the beamline from any debris,

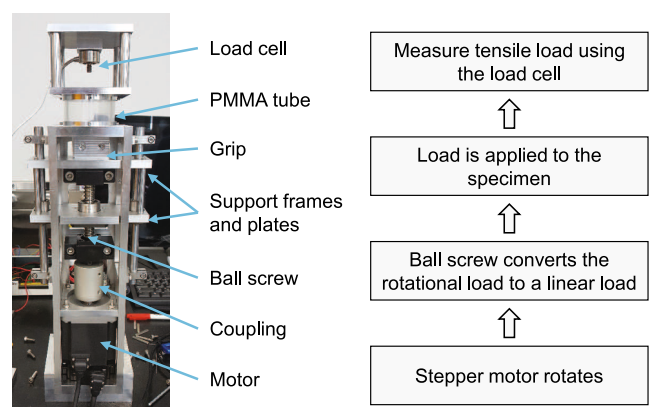


Fig. 7. Tensile loading frame with the load application mechanism. (For interpretation of the references to colour in this figure legend, the reader is referred to the web version of this article.)

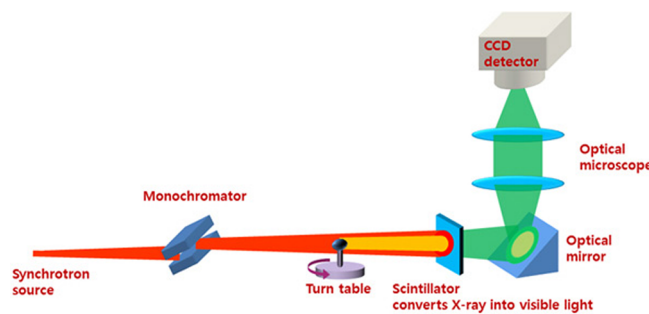


Fig. 8. Schematic illustration of the X-ray imaging system in the beamline 6C [25]. (For interpretation of the references to colour in this figure legend, the reader is referred to the web version of this article.)

potentially falling off from the specimen during the test. The PMMA material is a transparent thermoplastic, generally having a low density, that does not significantly deteriorate the X-ray intensity. The present load frame was installed with a 5-mm thick PMMA tube, which resulted in about 70% of transmission efficiency. The motor was placed far from the specimen to avoid potential vibratory disturbance from the operating motor. The motor located at the bottom also served as a base weight for the slender load frame. The motion controller based on the PID controller carried out a feedback control on the motor to maintain the user-specified loading rate during the experiment. The load data was recorded from the piezo-electric type load cell installed in the top part of the loading.

4.2. In situ experimentation using a synchrotron light source

Fig. 8 illustrates the X-ray imaging system of Beamline 6C. The synchrotron light was first monochromated before the beam passed through the sample. A double-multilayer monochromator (DMM) and a double-crystal monochromator (DCM) are the two typical monochromators used in an optics hutch at synchrotron facilities. While the DCM delivers a highly monochromatic beam ($\Delta E/E \approx 10^{-4}$), the DMM provides an energetically broader beam ($\Delta E/E \approx 10^{-2}$) and thus a much higher photon flux is delivered on the sample [23,24]. Beamline 6C at PAL was equipped with the DMM and set to provide 27 keV X-rays for the present *in situ* testing. The tensile testing device was mounted on the turn table as shown in Fig. 8 and its position was adjusted using the precision positioning stage to locate the center of the specimen on the beam path. The X-ray beam passed through the specimen was converted to visible light by the scintillator as illustrated in Fig. 8. Scintillator materials absorb the energy of ionizing radiation and reemit the absorbed energy in the form of visible light. PAL utilized a 100- μm thick CdWO₄ filter for the scintillation. The converted visible light was detected by the charge-coupled device (CCD) camera. In the present experimentation, the distance from the sample to the detector was set to 110 mm. The position of the focal point was decided on the magnification level. For the single-edge notched tension (SENT) test, we used 20 \times lens that resulted in the pixel size of 0.45 μm with the field of view (FOV) having the width of 1.8 mm and the height of 1.2 mm, which was fine and large enough to observe the initiation and propagation of cracks near the notch tip.

X-ray images were taken at the six loading steps as indicated in Fig. 9. The six positions in Fig. 9 correspond to 15%, 25%, 35%, 45%, 57% and 68% of the failure strength of the SEN specimen. The failure strength was measured from a separate test and found to be 893 MPa. Displacement-controlled loading was applied to the specimen with the loading rate of 0.1 mm/min and a specific displacement was maintained while X-ray images were being taken within 2 minutes. At each of the seven steps, X-ray projection images were recorded at every 0.15° as the testing instrument was rotated stepwise through the total angular range of 180 degrees.

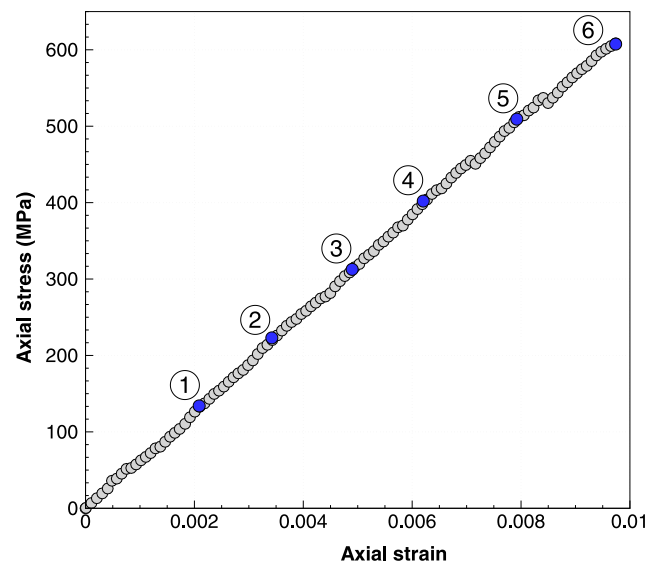
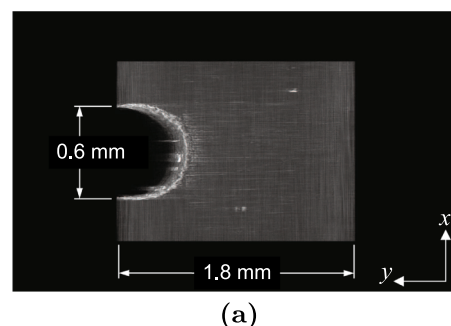
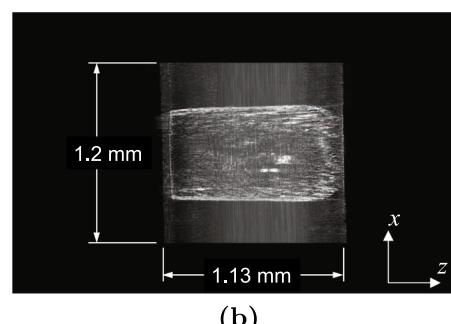


Fig. 9. Stress-strain response of [90₂/0₂]s specimen with a single edge notch. Points 1 to 6 indicate the loads when the X-ray images were taken. (For interpretation of the references to colour in this figure legend, the reader is referred to the web version of this article.)

In general, X-ray radiography utilizes different radiation absorption capabilities of materials. The energy absorbed by a particular object is mainly dependent on its atomic number and density, eventually correlated with a specific gray-scale value in a radiograph. The higher the density of the material, the darker it will be imaged on the radiograph. In the present experiment, solids (matrix and fibers) and vacancies (cracks, voids and air), having different densities, thus could be visually recognized in the series of radiographs by the corresponding grayscale intensities. The X-ray projection images (radiographs) of the SEN specimen were used to generate two-dimensional (2D) tomographic slices (tomograms), using a commercial reconstruction software package, Octopus Reconstruction [26]. The 2D slice images were further processed to create the three-dimensional (3D) volume image of the SENT



(a)



(b)

Fig. 10. 3D volume images of the unloaded specimen near the notch tip.

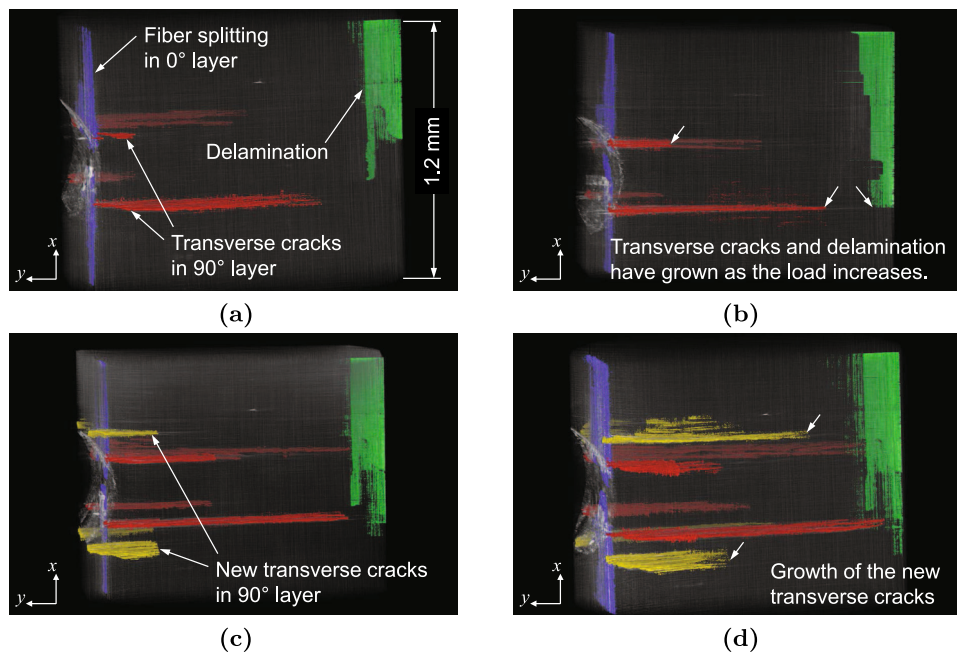


Fig. 11. 3D images of the fractured specimen at various loading stages (a) 35% of the failure load (b) 45% of the failure load (c) 57% of the failure load (d) 68% of the failure load. (For interpretation of the references to colour in this figure legend, the reader is referred to the web version of this article.)

specimen, using the commercial visualization software, Amira Software [27].

5. Results and discussions

5.1. Failure progression at multiple loading steps

Fig. 10 shows the rendered 3D image of the specimen around the notch before it is loaded. We have narrowed the FOV size with the dimensions shown in Fig. 11 since the fracture behavior at the notch tip is of great interest in the present work. Various failure modes near the

notch tip and their progressions with the increasing load are detected as shown in Fig. 11. As can be seen in Fig. 11(a), the transverse matrix cracks, colored in red, are found in the 90° plies at the notch tip with the fiber directional splitting (blue) in the 0° plies. Delamination (green) is also observed on the far side of the notch. Unfortunately, the initiation sequence between the two cracks at the notch tip is unknown since they have occurred between 25% and 35% of the failure load, at which the X-ray scanning is not performed. If the specimen is scanned at much more loading steps between 25% and 35% of the failure load, the initiation sequence of the two cracks might be detected. However, since the two cracks are expected to initiate almost simultaneously due

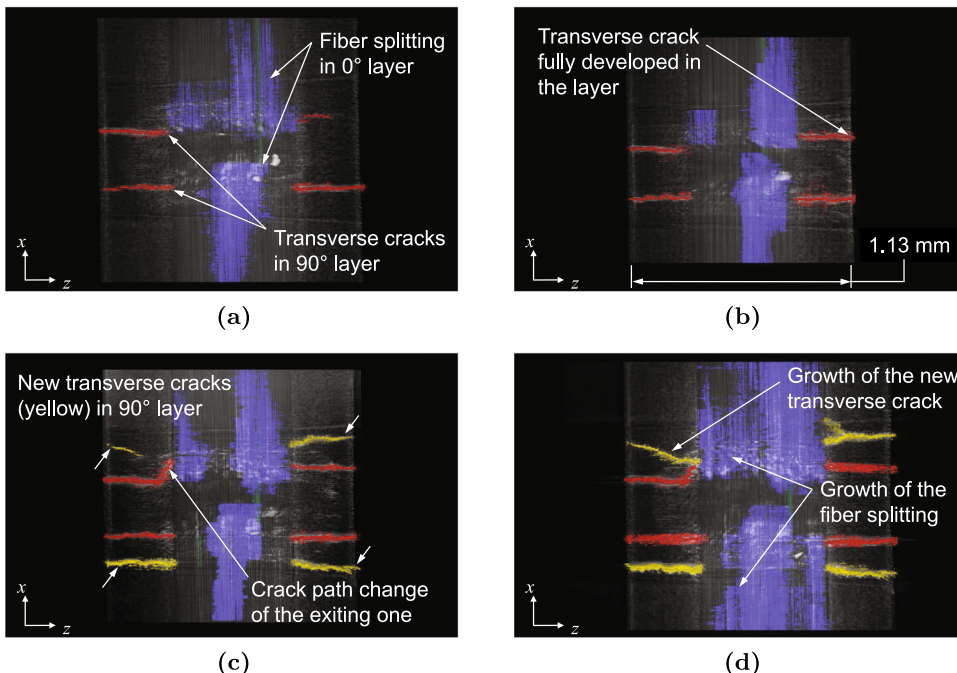


Fig. 12. Failure progression displayed from a different angle of Fig. 11 at the same loading stages (a) 35% of the failure load (b) 45% of the failure load (c) 57% of the failure load (d) 68% of the failure load. (For interpretation of the references to colour in this figure legend, the reader is referred to the web version of this article.)

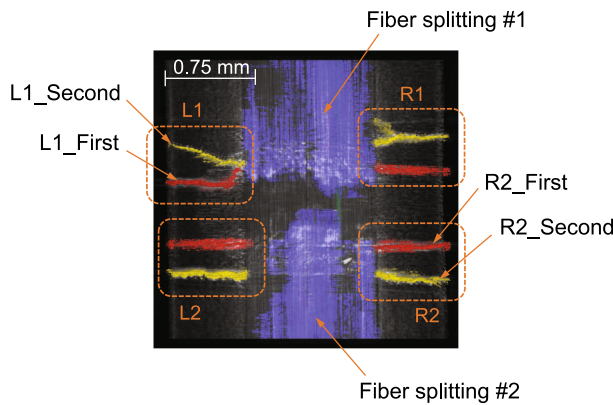


Fig. 13. Notations of the transverse cracks in the regions T1 and T2. Fiber directional cracks in the 0° layers are denoted with #1 and #2 according to their locations with respect to the mid-plane of the specimen. (For interpretation of the references to colour in this figure legend, the reader is referred to the web version of this article.)

to the symmetry of the specimen, numerous steps between 25% and 35% should be needed to detect the sequential crack initiation. Excessive X-ray scans means numerous interruptions during the tensile test. This would increase experimental time dramatically and potentially contaminate the tensile test results.

The initiation of the additional transverse cracks (yellow) in the 90° layers is individually detected as the load increases from 45% to 57% of the peak load. It is interesting to note that all the transverse matrix cracks in the 90° layers are formed almost symmetrically with respect to the central plane of the sample. As the load is further increased, the transverse matrix cracks and the longitudinal splitting are continuously growing as shown in Figs. 11 and 12. Fig. 12 shows the same fractured specimen from a different viewpoint. The fiber directional splitting mode is more clearly observed in Fig. 12. It seems that the growth of the splitting is greatly influenced by the transverse cracks in the 90° layer. In Fig. 12, the first splitting on the right side of the 0° layers becomes longer after the transverse crack on the 90° layer is fully developed over the entire thickness of the layer. Similar growing behavior of the splitting is observed with the combination of the new transverse crack (yellow).

5.2. Quantitative analysis of interacting failure modes

Interactions between the various failure modes are quantitatively examined with the 3D volume visualization. For the transverse cracks occurring in the 90° layers, four regions are first designated as shown in Fig. 13. The prefix "L" and "R" denote the 90° layers on the left and right hand sides, respectively. The numbers "1" and "2" indicate the locations of the cracks with respect to the mid-plane of the sample. The existing and the additional cracks are distinguished with the suffices "first" and "second", respectively, following the corresponding region legends (see Fig. 13 for examples). The longitudinal splitting failure modes are denoted with #1 and #2 depending on their locations in a similar manner. Fig. 14(a) and (b) compare the growth of the transverse cracks occurring in the left and right 90° layers, respectively, with a variance of the applied load. As can be seen in Fig. 14, the first transverse matrix cracks (solid lines) are continuously growing as the applied load increases for both cases. However, the growth rates of the existing cracks in the regions of L2 and R1 are fairly reduced after the emergence and rapid growth of the second ones (dash-dotted lines) in the same areas. In general, once a crack in a material is initiated, a significant amount of energy is released through the fracture process and highly concentrated stresses in the cracking area are redistributed. When two cracks are closely developed in the direction transverse to tensile loading, the stresses accumulated in the area situated between

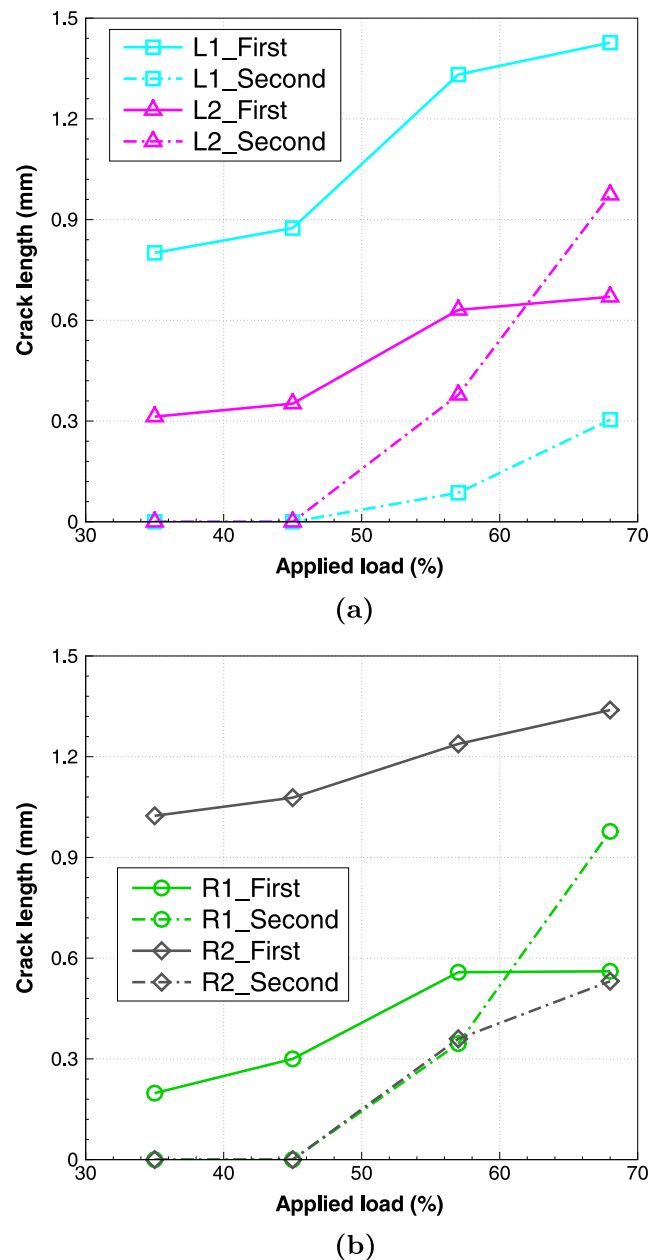


Fig. 14. Interactive progression of the first and second transverse cracks. (For interpretation of the references to colour in this figure legend, the reader is referred to the web version of this article.)

the two neighboring cracks are rapidly relaxed. In the present experiment, the existing cracks (red ones in Fig. 12) are to be in the stress relaxation region due to the emergence of the second transverse cracks (yellow ones in Fig. 12), resulting in the slower fracture process. The second cracks are still stressed due to the constant supply of the far-field loading. Their crack opening displacements (CODs) are increasing as shown in Fig. 15 while the first cracks are even closing. Fig. 16 clearly shows this interaction between the first and second transverse cracks in the region of L2. Fig. 16(a) and (b) are the tomograms sectioned at the crack tips in L2 region at different loading steps. As can be seen in Fig. 16(a) and (b), the COD of the first crack decreases while the second crack is opening with the increasing load. It again implies that the stress relaxation occurs around the regions of the first cracks and the areas locally lose the load carrying capability as a result of the emergence of the second cracks.

It is interesting to note that the second cracks in the regions of L1

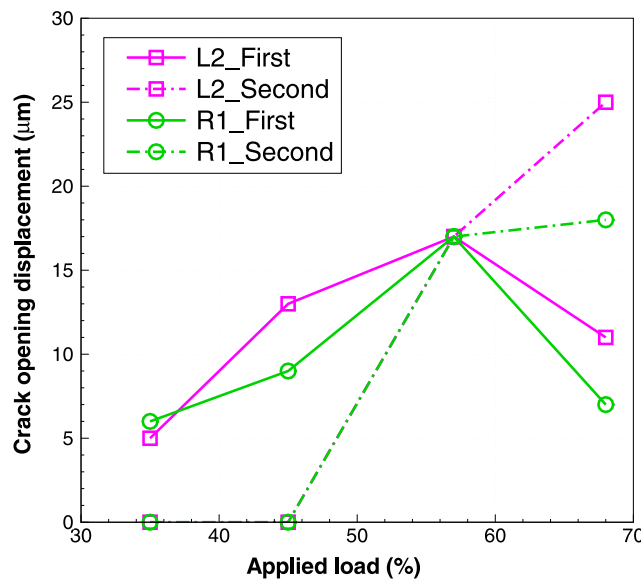


Fig. 15. Interactive progression of the first and second transverse cracks. (For interpretation of the references to colour in this figure legend, the reader is referred to the web version of this article.)

and R2 are not growing as rapidly as the others as shown in Fig. 14(a) and (b), respectively. The aforementioned interactive progression of the sequential transverse cracks is only clearly observed in the L2 and R1 regions. Indeed, there exists another failure mode in the 0° layers that may interact with the transverse cracks in the 90° layers. However, the fiber directional splitting failure does not exist near the L2 region (see Fig. 12(d)) and has been already fully developed before the transverse cracks grow in the R1 region (see Fig. 12(a)). Hence, the effect of the splitting failure mode could be minimal on the propagation of the transverse cracks in the particular areas. On the contrary, near the regions of L1 and R2, the splitting failure is growing simultaneously with the adjacent transverse cracks and thus they essentially influence each other. Fig. 17 compares the growth of the transverse cracks in the areas with the longitudinal splitting failure. Since the tip of the splitting exists beyond the FOV, the splitting growth is characterized by its volume or volume fraction, defined as the volume occupied by the particular cracking mode divided by the entire volume of the unloaded sample in the FOV region. The volumes can be easily obtained by counting the number of voxels. As can be seen in Fig. 17, for both cases, the fiber-direction splitting grows very rapidly, resulting in the slower fracture processes for the second transverse cracks. This quantitative description is also observed from the 3D volumetric images in Fig. 11(a) through (d).

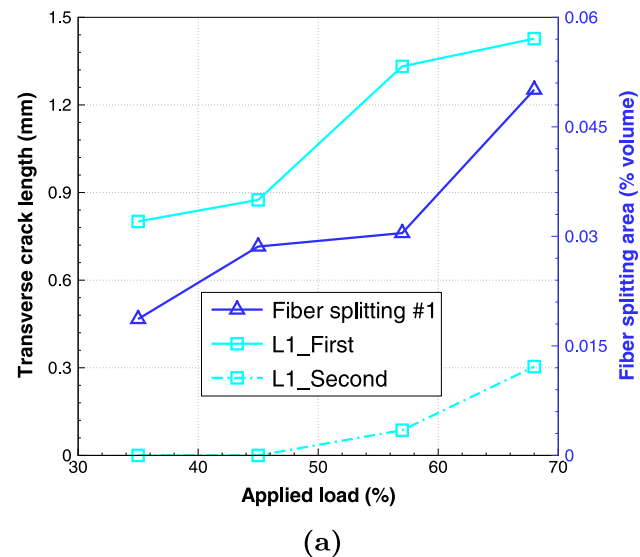


Fig. 17. Interactions between the fiber-direction splitting and transverse fracture modes. (For interpretation of the references to colour in this figure legend, the reader is referred to the web version of this article.)

6. Conclusions

The progression of multiple failure modes that are interacting and competing with each other in the laminated composite specimen is

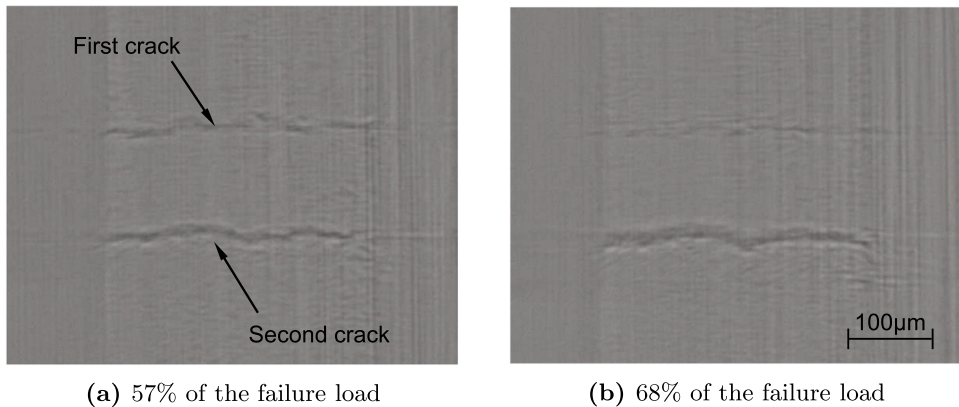


Fig. 16. Changes of the crack opening displacements for the first and second cracks in L2 region.

observed *in situ* and quantitatively analyzed through synchrotron X-ray tomography and a digital image correlation technique. The single-edge notched symmetric cross-ply laminate is utilized to observe the complex fracture behavior near the notch tip. Transverse cracks, longitudinal cracks and delaminations, which are common concerns of composite structures, are observed and their interactions are quantitatively examined. The competing behavior between existing and emerging cracks are analyzed by measuring their growing lengths and opening displacements from 3D CT images obtained through synchrotron radiation computed tomography. Stress redistribution and relaxation due to the series of transverse cracks are directly measured from the DIC analysis. The present *in situ* experiment results provides more informative insight for understanding the fracture behavior occurring inside the heterogeneous materials and can serve as a benchmark data to validate a predictive numerical model.

Declaration of Competing Interest

The authors certify that we have NO affiliations with or involvement in any organization or entity with any financial interest (such as honoraria; educational grants; participation in speakers' bureaus; membership, employment, consultancies, stock ownership, or other equity interest; and expert testimony or patent-licensing arrangements), or non-financial interest (such as personal or professional relationships, affiliations, knowledge or beliefs) in the subject matter or materials discussed in this manuscript.

Acknowledgement

The authors are grateful for the financial support from Lockheed Martin through the Republic of Korea Science, Technology and Research (RoKST&R) program in the year of 2015. This work is also supported by Basic Science Research Program through the National Research Foundation of Korea (NRF) funded by the Ministry of Education (Grant No.: 2017R1D1A1B03035011). The authors are greatly indebted to Dr. Jaehong Lim at PAL for his support in the *in situ* test.

References

- [1] Deloitte Touche Tohmatsu Limited. Automotive and composite materials: current state and forecast. Paris, France: JEC Composites Publication; 2018.
- [2] Ng WH, Salvi AG, Waas AM. Characterization of the *in-situ* non-linear shear response of laminated fiber-reinforced composites. *Compos Sci Technol* 2010;70(7):1126–34.
- [3] Bernachy-Barbe F, Gélébart L, Bornert M, Crépin J, Sauder C. Characterization of SiC/SiC composites damage mechanics using digital image correlation at the tow scale. *Compos A* 2015;68:101–9.
- [4] Yu B, Blanc R, Soutis C, Withers PJ. Evolution of damage during the fatigue of 3D woven glass-fibre reinforced composites subjected to tension-tension loading observed by time-lapse X-ray tomography. *Compos A* 2016;82:279–90.
- [5] Correa E, Valverde MI, Velasco ML, París F. Microscopic observations of inter-fibre failure under tension. *Compos Sci Technol* 2018;155:213–20.
- [6] Lomov SV, Ivanov DS, Truong TC, Verpoest I, Baudry F, Bosche V, et al. Experimental methodology of study of damage initiation and development in textile composites in uniaxial tensile test. *Compos Sci Technol* 2008;68:2340–9.
- [7] Daggumati S, De Baere I, Van Paepeng W, Degrieck J, Xu J, Lomov SV, et al. Local damage in a 5-harness satin weave composite under static tension: Part I - Experimental analysis. *Compos Sci Technol* 2010;70:2340–9.
- [8] Carvalho NV, Pinho ST, Robinson P. An experimental study of failure initiation and propagation in 2D woven composites under compression. *Compos Sci Technol* 2011;71:1316–25.
- [9] Stock SR. Recent advances in X-ray microtomography applied to materials. *Int Mater Rev* 2013;53(3):129–81.
- [10] Sakdinawat A, Attwood D. Nanoscale X-ray imaging. *Nat Photon* 2010;4:840–8.
- [11] Buffiere JY, Maire E, Adrien J, Masse JP, Boller E. *In situ* experiments with X ray tomography: an attractive tool for experimental mechanics. *Exp Mech* 2010;50(3):289–305.
- [12] Moffat AJ, Wright P, Helfen L, Baumbach T, Johnson G, Spearing SM, et al. *In situ* synchrotron computed laminography of damage in carbon fibre-epoxy [90/0]s laminates. *Scri Mater* 2010;62(2):97–100.
- [13] Wright P, Moffat A, Sinclair I, Spearing SM. High resolution tomographic imaging and modelling of notch tip damage in a laminated composite. *Compos Sci Technol* 2010;70(10):1444–52.
- [14] Scott AE, Mavrogordato M, Wright P, Sinclair I, Spearing SM. *In situ* fibre fracture measurement in carbon-epoxy laminates using high resolution computed tomography. *Compos Sci Technol* 2011;71(12):1471–7.
- [15] Garcea SC, Mavrogordato MN, Scott AE, Sinclair I, Spearing SM. Fatigue micro-mechanism characterization in carbon fibre reinforced polymers using synchrotron radiation computed tomography. *Compos Sci Technol* 2014;99(30):23–30.
- [16] Hufenbach W, Bohm R, Gude M, Berthel M, Hornig A, Rucevskis S, et al. A test device for damage characterization of composites based on *in situ* computed tomography. *Compos Sci Technol* 2012;72(12):1361–7.
- [17] Bale HA, Haboub A, Macdowell AA, Nasiatka JR, Parkinson DY, Cox BN, et al. Real-time quantitative imaging of failure events in materials under load at temperatures above 1600 degrees C. *Nan Mater* 2013;12(1):40–6.
- [18] Sket F, Rodriguez-Hortal M, Molina-Aldareguia JM, Liorca J, Maire E, Requena G. *In situ* tomographic investigation of damage development in ± 45° carbon fibre reinforced laminates. *Mater Sci Technol* 2015;31(5):587–93.
- [19] Garcea SC, Wang Y, Withers PJ. X-ray computed tomography of polymer composites. *Compos Sci Technol* 2018;156:305–19.
- [20] Wang Y, Garcea SC, Withers PJ. 7.6 Computed tomography of composites. *Comprehensive Compos Mater II* 2018;7:101–18.
- [21] Ji W, Boyd S, Joseph APK, Waas AM. Single edge notch tension test on cross-ply laminated composites for intralaminar fracture properties. In: SciTech 2014, 55th AIAA / ASME / ASCE / AHS / ASC Structures, Structural Dynamics, and Materials Conference, National Harbor, MD, January 13–17, 2014, number AIAA-2014-0852.
- [22] Yang QD, Schesser D, Niess M, Wright P, Mavrogordato MN, Sinclair I, et al. On crack initiation in notched, cross-plyed polymer matrix composites. *J Mech Phys Solids* 2015;78:314–32.
- [23] Müller BR, Lange A, Hentschel MP. Synchrotron radiation refraction tomography. In: Green RE, Djordjevic BBB, Hentschel MP, editor. Nondestructive Characterization of Materials XI: Proceedings of the 11th International Symposium, Berlin, Germany, June 24–28, 2002, Springer-Verlag Berlin Heidelberg, Germany, 2003, pp. 167–176.
- [24] Wilde F, Ogurreck M, Greving I, Hammel JU, Beckmann F, Hipp A, et al. Micro-CT at the imaging beamline P05 at PETRA III. *AIP Conf Proc* 2016;1741(1):030035.
- [25] Pohang Accelerator Laboratory, pal.postech.ac.kr/paleng/bl/6C/ [accessed November 2018].
- [26] Octopus Imaging Software, Ver. 8, XRE NV, Gent, Belgium; 2017.
- [27] Amira Software, Ver. 6.2, Thermo Fisher Scientific, Hillsboro, OR, United States, 2017.